Catalytic boosting on AuCu bimetallic nanoparticles by oxygen-induced atomic restructuring

Taek-Seung Kim [a,b,1], Hyuk Choi [c,1], Daeho Kim [a,b], Hee Chan Song [a,b], Yusik Oh [a], Beomgyun Jeong [d], Jouhahn Lee [d], Ki-Jeong Kim [e], Jae Won Shin [b], Hye Ryung Byon [a], Ryong Ryoo [f], Hyun You Kim [c,*], Jeong Young Park [a,b,**]

[a] Department of Chemistry, Korea Advanced Institute of Science and Technology (KAIST), Daejeon 34141, Republic of Korea
[b] Center for Nanomaterials and Chemical Reactions, Institute for Basic Science (IBS), Daejeon 34141, Republic of Korea
[c] Department of Materials Science and Engineering, Chungnam National University, Daejeon 34134, Republic of Korea
[d] Research Center for Materials Analysis, Korea Basic Science Institute (KBSI), Daejeon 34133, Republic of Korea
[e] Beamline Research Division, Pohang Accelerator Laboratory, Pohang 37674, Republic of Korea
[f] Department of Energy Engineering, Korea Institute of Energy Technology (KENTECH), Naju, Jeonnam 58330, Korea

ARTICLE INFO

ABSTRACT

Understanding the structure-activity relationship over silica-supported Au-based bimetallic nanocatalysts in CO oxidation is essential in elucidating active sites and catalytic mechanisms. Here, we uncover that structure-activity relationship over a silica-supported 10 nm sized AuCu bimetallic model nanocatalyst for CO oxidation. Oxygen–induced atomic restructuring of AuCu nanocrystals is comprehensively investigated using combined *operando* spectroscopic and microscopic techniques, including near-ambient-pressure X-ray photoelectron spectroscopy, diffuse reflectance infrared Fourier-transform spectroscopy, and environmental transmission electron microscopy. We show that the formation of CuO_x/Au heterostructure gives rise to the enhancement of catalytic activity for CO oxidation. The formation of the reactive heterostructure on catalysis was rationalized by density functional theory calculation. Our results indicate that intermediate heterostructure with a metal-oxide interface leads to strong electronic coupling between catalyst and support (*i.e.*, electronic metal-support interaction effect).

1. Introduction

CO oxidation is a useful reaction in industrial applications, such as automobile catalytic converters and selective elimination of CO in the hydrogen feed for proton exchange membrane fuel cells, which follows a simple pathway ($2CO + O_2 \rightarrow 2CO_2$) with no selectivity issue [1–3]. Hence, CO oxidation is one of the most important model heterogeneous catalytic reactions in surface science [4,5] and has attracted attention as a fundamental model study to shed light on these scientific phenomena.

The transition between two structural modifications of the Pt (110) *via* atomic rearrangement during the CO oxidation reaction was suggested by G. Ertl [6,7]. Understanding the atomic rearrangement on catalysis is important to elucidate the active sites for the CO oxidation reaction on monometallic and bimetallic nanocatalysts [8–10]. To

achieve thermodynamic stability in various adsorbates and temperature environments, two types of atoms in the bimetallic nanocatalyst undergo atomic restructuring and then form specific nanostructures [11, 12]. For example, the AuPd bimetallic catalysts form a AuPd alloy with Pd skin and Au core structure under CO oxidation conditions, due to the strong binding energy of Pd atoms with CO molecules [13]. In another example, the CoPd bimetallic nanocatalyst shows bimetallic synergy by forming a CoO_x–Pd interfacial structure *via* atomic rearrangement during the reaction, due to the strong binding energy of Co atoms with O_2 molecules, which in turn promotes the CO oxidation kinetics [9]. The bimetallic synergy of the CoPd nanocatalyst is associated with the electronic metal–oxide interaction (EMSI) concepts, which were generally introduced in the mixed catalyst system [14–16]. In other words, the atomic rearrangement of bimetallic nanocatalysts could present a

---

platform to understand the EMSI effect for CO oxidation.

Supported AuCu bimetallic nanocatalysts are one of the most widely used in heterogeneous catalytic applications (*e.g.*, CO oxidation, ethanol oxidation, electrochemical CO_2 reduction) among the Au-based bimetallic nanocatalysts [17–19], making it necessary to understand the fundamentals of the structure-activity relationship for CO oxidation catalysis on the supported AuCu bimetallic nanocatalysts. In particular, it has been reported that these nanocatalysts show segregation phenomena under different thermodynamic conditions [20–22]. This indicates that the AuCu bimetallic nanocatalysts with the atomic rearrangement phenomenon could be fascinating candidates for uncovering the influence of the EMSI effect on Au nanocatalysis. The earlier study showed the atomic restructuring tendency of Cu atoms induced by O adsorption on the two crystallographic orderings of AuCu alloy, such as face-centered cubic (fcc) AuCu (disordered alloy) and face-centered tetragonal (fct) AuCu (ordered alloy) [20]. Additionally, Bauer et al. also experimentally elucidated the formation of oxygen-driven CuO_x intermediate structure on the Au–Cu nanocrystals using *ex situ* investigations, which makes the AuCu catalyst more active for ethanol oxidation reactions [18]. The bimetallic synergy of the AuCu alloy has been studied by many researchers, but the evolution mechanism of intermediate structure by atomic restructuring and its exact role during the CO oxidation reaction remain challenging issues.

As state-of-the-art micro/spectroscopy techniques have developed, sophisticated *in situ/operando* characterization at atomic scale during the catalytic reaction has become possible [23–25]. It facilitates tracking the real-time intermediate states during the reaction and serves the active site information, which has led to advances in surface chemistry for heterogeneous catalysis. Recently, Kim et al. elucidated the bimetallic synergy in Pt–Ni nanocatalysts using combined near ambient-pressure XPS (NAP-XPS) and environmental transmission electron microscopy (E-TEM) studies; they found that the $Pt-NiO_x$ interfacial structure formation is driven by reconstructing the catalyst in a CO oxidation environment [10]. In the Au–Cu nanocrystal system, Luo et al. observed atomic-scale structural change of AuCu NP on ceria support during the CO oxidation reaction using E-TEM, which provides the information for atomic-scale visualizing intermediate structure ($Cu_2O/AuCu$) formation by atomic restructuring, but the CO conversion kinetics on the intermediate structure are not discussed in the experimental reaction study [21]. To further understand the catalytic active sites, we need to obtain the chemical information (*e.g.*, catalytic performance, chemical binding and vibrational frequency) during CO oxidation reaction using *in situ/operando* spectroscopic analysis as well as microscopic observation.

Here, we elucidate the atomic-scale evolution of AuCu nanocrystals during an oxidation reaction using *in situ/operando* investigations and DFT calculation; its catalytic role was unveiled during the CO oxidation reaction. To concentrate on the EMSI effect without the Au size effect [26], we prepared AuCu, Au, and Cu model nanocrystals of about 10 nm. The AuCu catalyst pretreated in O_2 conditions shows enhanced catalytic performance compared to the pristine AuCu catalyst. To find the reason for this phenomenon of bimetallic synergy, sophisticated *in situ* surface analysis (by NAP-XPS) and a CO adsorption investigation (by diffuse reflectance infrared Fourier-transform spectroscopy, DRIFTS) were performed; this chemically elucidated the formation mechanism for CuO_x/Au heterostructure, which was rationalized by DFT calculation. The formation of CuO_x/Au heterostructure in O_2 conditions was observed in real-time using E-TEM. Then, the active site and reaction pathway for CO oxidation was uncovered by *operando* NAP-XPS measurement and DFT calculation. Our study offers an opportunity to understand the EMSI effect more intuitively from the different points of view of the supported Au catalyst system.

2. Experimental

2.1. Synthesis of AuCu, Au, and Cu NPs

2.1.1. Synthesis of AuCu NPs

In a typical synthesis of Au–Cu nanocrystals, 45 mg (0.12 mmol) of gold(III) chloride trihydrate (HAuCl$_4$·3 H$_2$O, 97%, Sigma–Aldrich) and 13 mg (0.05 mmol) of copper(II) acetylacetonate [Cu(acac)$_2$, 99.9%, Sigma–Aldrich] were dissolved in 5 ml of 1-octadecene (90%, Alfa Aesar) containing 100 mg of 1,2-hexadecanediol (98%, TCI), 1 ml of oleylamine (70%, Sigma–Aldrich), and 1 ml of oleic acid (99%, Sigma–Aldrich) in a 50 ml three-neck round-bottom flask. The flask was evacuated for 30 min with vigorous stirring at room temperature (RT). The solution was heated to 393 K and kept for 30 min, then heated to 553 K. The evacuated flask was purged with Ar gas from 453 K for 10 min. The solution was kept at 553 K for 30 min with vigorous stirring. After the reaction, the solution cooled down to RT. The colloidal suspension was diluted to 50 ml of toluene: isopropanol (1:5 vol. ratio) mixture and centrifuged at 6500 rpm for 10 min twice, repeatedly. Then, the suspension was re-dispersed in 20 ml of hexane and centrifuged at 2000 rpm for 10 min to eliminate undispersed chemical species. Then, as-synthesized AuCu NPs were re-dispersed in 20 ml of hexane, referred to as the pristine AuCu NPs.

2.1.2. Synthesis of Au NPs

In a typical synthesis of Au NPs, 65 mg (0.17 mmol) of gold(III) chloride trihydrate (HAuCl$_4$·3 H$_2$O, 97%, Sigma–Aldrich) was dissolved in 5 ml of 1-octadecene (90%, Alfa Aesar) containing 100 mg of 1,2-hexadecanediol (98%, TCI), 1 ml of oleylamine (70%, Sigma–Aldrich), and 1.2 ml of oleic acid (99%, Sigma–Aldrich) in a 50 ml three-neck round-bottom flask. The flask was evacuated for 30 min with vigorous stirring at RT, and the evacuated flask was purged with Ar gas. The solution was heated to 393 K and kept for 30 min. After the reaction, the solution cooled down to RT. The purification process was the same for the pristine AuCu NPs. Then, as-synthesized Au NPs were re-dispersed in 20 ml of hexane.

2.1.3. Synthesis of Cu NPs

For synthesis of Cu NPs, 100 mg (0.38 mmol) of copper(II) acetylacetonate [Cu(acac)$_2$, 99.9%, Sigma–Aldrich] were dissolved in 5 ml of oleylamine (70%, Sigma–Aldrich) in a 50 ml three-neck round-bottom flask. The mixed solution was heated to 353 K, then the flask was evacuated for 30 min. The evacuated flask was purged with Ar gas. The solution was heated to 493 K, and the solution was kept at this temperature for 2 hr with vigorous stirring. After the reaction, the solution cooled down to RT. The purification process was the same with that of pristine AuCu NPs. Then, as-synthesized Cu NPs were re-dispersed in 20 ml of hexane.

2.2. Characterizations

The chemical composition of pristine AuCu NPs was examined using inductively coupled plasma mass spectroscopy (ICP-MS; 7700 S ICP-MS, Agilent). Crystallinity investigation for all samples was carried out by X-ray diffractometer (XRD; Ultima IV, Rigaku) with Cu Kα ($\lambda = 1.5418$ Å). The absorbance spectrum of all samples was obtained using an ultraviolet–visible spectrophotometer (UV–Vis; UV-2600, SHIMADZU). The images of AuCu, Au, and Cu monolayer film on SiO$_2$ substrate were obtained using field emission scanning electron microscopy (FESEM; Magellan400, FEI company). *Ex situ* chemical binding information was investigated by X-ray photoelectron spectroscopy (XPS; K-alpha, Thermo VG Scientific) with Al Kα (E = 1486.74 eV). *Ex situ* investigations of morphology and chemical information for pristine AuCu NPs were performed using transmission electron microscopy, high-angle annular dark-field scanning transmission electron microscopy, and energy dispersive X-ray spectroscopy (TEM, HAADF-STEM, and EDS; Titan

cubed G2 60–300, FEI) at 300 kV. The formation of oxygen vacancy in the pristine and O_2-AuCu NPs was measured using electron paramagnetic resonance spectroscopy (EPR; JES-FA100, Jeol).

2.3. Measurement of catalytic activity for CO oxidation

To prepare the sample for the catalytic reaction, the O_2-AuCu, pristine AuCu, Au, and Cu NPs were deposited on SiO_2 substrate using a spin coater (ACE-200, Dong ah trade corp.). In the ultra-high vacuum chamber (1 L), the catalytic reaction was performed with a base pressure of 10^{-8} Torr, which was evacuated by vacuum pumps (*e.g.*, rotary and turbomolecular pumps) and isolated with a gate valve. Then, the batch reactor chamber was charged with 40 Torr CO and 100 Torr O_2 as the reactant gases and 620 Torr He as the balancing gas. All the mixtures of reactant gas were circulated continuously through the line using a Metal Bellows recirculation pump (MB-41) at 2 L min^{-1}. After circulation for 20 min in order to achieve equilibration of the gas mixtures, a gas chromatograph (GC; DS6200 Gas Chromatograph, Donam Instrument Inc.) combined with a thermal conductivity detector and stainless-steel molecular sieve 5 A (6 ft long and 1/8" outer diameter) was operated to classify the reactants (CO and O_2) and product (CO_2) for catalytic investigation. CO conversion was obtained in the region of reaction temperatures (460–540 K). The CO conversion rate was reported as turnover frequency (TOF). The active site area was obtained by geometric consideration, because the real and apparent surface areas exhibited similar values of active sites on a thin film catalyst [27,28], which is an approximate way to measure the turnover frequency (TOF) by assuming that all surface sites are active. We estimated the apparent surface area by considering the surface coverage of the catalysts (*e.g.*, O_2-AuCu, AuCu, Au, and Cu NPs) on a SiO_2 substrate, based on the high-resolution SEM images. The coverage of O_2-AuCu, pristine AuCu, Au, and Cu catalysts on SiO_2 substrate are 3.21%, 5.87%, 6.41%, and 14.44%, respectively. All the TOF data were calculated by measuring the CO conversion rate in the low conversion region (less than 20%), presuming that the initial reaction rate was in a kinetically controlled regime.

2.4. Synchrotron-based and Al Kα in situ/operando NAP-XPS measurements

Synchrotron-based X-ray photoemission spectra of pristine AuCu NPs were obtained at the endstation of 8A2 beamline in the Pohang Light Source (PLS-II), Republic of Korea [29]. The NAP-XPS setup consists of an analysis chamber, including back-filling configuration, equipped with a PHOIBOS 150 hemispherical electron analyzer (SPECS). For *in situ* NAP-XPS measurement, the analysis chamber was backfilled with O_2 (5 N) gas molecules up to 0.2 mbar as a reactant for the oxidation reaction. The incident photon energies of each obtained Cu 2*p*, O 1 *s*, and Au 4 *f* core-level spectrum were adjusted to 1000, 645, and 250 eV to achieve similar surface sensitivity, collecting escaping photoelectrons from the topmost surface (*i.e.,* kinetic energy $\cong$ 100 eV; probing depth $\leq$ 10 Å). Core-level spectra in the regions of Cu 2*p* and O 1 *s* were collected with an energy step of 0.1 eV and pass energy of 50 eV.

The Al Kα *in situ/operando* NAP-XPS spectra of pristine AuCu NPs were measured using the NAP-XPS technique of the Advanced *in situ* Surface Analysis System (AiSAS) at the Korea Basic Science Institute (KBSI) in the Republic of Korea [30]. The custom-built NAP-XPS setup contains an *operando* high-pressure reaction cell, micro-focused X-ray source (Al$_{Kα}$, E = 1486.74 eV), and PHOIBOS 150 NAP hemispherical electron analyzer (SPECS). For *in situ* NAP-XPS measurement, the reaction cell was filled with O_2 (5 N) gas molecules up to 1 mbar as a reactant for the oxidation reaction. For *operando* NAP-XPS measurement, the reaction cell was filled with 0.4 mbar CO (5 N) and 1 mbar O_2 (5 N) gas molecules as reactants for the CO oxidation reaction. Core-level spectra in the regions of Cu 2*p*, O 1 *s*, and Au 4 *f* were collected with an energy step of 0.1 eV and pass energy of 40 eV.

All binding energy was calibrated with respect to the Fermi edge. For a detailed understanding of the obtained *operando* NAP-XP spectra, all peak in core-level Cu 2*p* and O 1 *s* were deconvoluted using Lorentzian asymmetric shape based on a Shirley-type background by CasaXPS package.

2.5. In situ DRIFTS measurement

Fourier-transform infrared spectrometer (FT-IR; Carry 660, Agilent) with the reaction cell, including diffuse reflectance optics (Harrick), a mercury cadmium telluride (MCT) detector, and ZnSe windows, was used to measure the *operando* DRIFTS analysis. The MCT detector operates every 32 scans with a resolution of 4 cm^{-1}. During all DRIFTS measurements, Helium (He) gas was used to purge the inside of the spectrometer. The temperature in the reaction cell was adjusted by heater, and gas flow rate was controlled by mass flow controllers (MFC; BROOKS Instrument).

Th pristine AuCu, Au, and Cu NPs were supported on the commercial SiO_2 NPs (SiO_2, 99.5%, Sigma–Aldrich) with a size of 10–20 nm for DRIFTS investigation. The stainless-steel mesh mechanically pressed with pristine AuCu, Au, and Cu/SiO_2 catalysts was prepared to prevent contamination in the reaction cell. To examine the vibrational frequency of adsorbed CO on the catalyst surface, the samples were exposed to 50 ml min^{-1} of CO/He gas mixture flow (CO/He feed, 1:4 v/v) conditions for 30 min, and then inside the reaction cell was purged with pure He gas flow conditions for 1 hr. For *operando* DRIFTS investigation, we carried out the CO adsorption test of the pristine AuCu/SiO_2 catalyst before and after the oxidation reaction (50 ml min^{-1} of O_2 gas flow) for 1 hr at 573 K. All CO adsorption DRIFT spectra were obtained at room temperature.

2.6. E-TEM measurement

For an *in situ* observation, an aberration-corrected environmental TEM (Titan E-TEM G2, FEI) was operated at 300 kV using a Fusion heating holder (Protochips inc.). For sampling, the pristine AuCu NPs were deposited on SiO_2 support particles with a diameter of 400 nm. The pristine AuCu/SiO_2 NPs were dropped on the Fusion heating holder, and then the holder was heated up from RT to 423 ℃ with a heating rate of 10 ℃/min in a vacuum and under 0.1 mbar of O_2 gas (Fig. 3a–c). Electron beam was blanked during the heating step to prevent beam irradiation effect.

Additionally, oleylamine-capped colloidal pristine AuCu NPs have an amorphous carbonaceous layer on the NP surface, marked by black arrows in Fig. 3a. This amorphous layer can disturb the real-time imaging of surface interaction between the surface of AuCu NP and O_2 molecules. For capturing the situation for atomic restructuring, the carbonaceous layer of targeted NP was minimized *via* irradiation of electron beam under 1 mbar of O_2 gas at RT, which, in turn, exhibits a clean Au–Cu NP surface, as shown in Video S1 and Fig. 3b and c [31,32].

2.7. Density functional theory calculations

We performed spin-polarized density functional theory (DFT) calculations using the Vienna Ab-initio Simulation Package (VASP) code [33]. The Perdew-Beck-Ernzerhof (PBE) [34] functional was applied to estimate the exchange-correlation energy. We employed the Hubbard-*U* formalism (DFT+U) [35] with U_{eff} of 5.2 eV [36,37] to appropriately treat the localized Cu-3*d* orbitals. The interaction between the ionic core and the valence electrons was described by the projector augmented wave method [38]. Valance electron wave functions were expanded in a plane-wave basis up to an energy cutoff of 400 eV. The Brillouin zone was sampled at the Γ-point for all calculations. The convergence criteria for the electronic structure and the atomic geometry were 10^{-4} eV and 0.05 eV/Å, respectively. We used the Methfessel-Paxton smearing function with a finite temperature width of 0.2 eV in order to improve

convergence of states near the Fermi level. The location and the energy of the transition states (TSs) were calculated with the climbing-image nudged elastic band method [39,40].

To calculate the energetics of Cu surface segregation, we used a $4 \times 4 \times 6$ Au$_3$Cu(100) substrate. We chose a (100) type slab model, which assures facile dynamic surface segregation of solute elements in Au-based alloys [41,42]. The Cu atoms within the upper four layers of the slab model were sequentially segregated to the surface layer, forming a Cu$_2$O and, eventually, a CuO NP with gas phase oxygen molecules, transforming the six-layered Au$_3$Cu slab model into a CuO/Au model. (Fig. S10). The bottom two layers of Au$_3$Cu were fixed during geometry optimization. We used a Cu$_{70}$O$_{70}$-slab supported on a wider $7 \times 5 \times 3$ Au(100) slab to study the mechanism of CO oxidation catalyzed by a CuO/Au type catalyst (Fig. S19). A specific size of Au(100) $7 \times 5 \times 3$ slab was selected to minimize the lattice mismatch between Au and CuO. A vacuum layer of 20 Å was introduced to avoid interactions between the periodic slabs.

3. Results and discussion

3.1. AuCu nanocatalyst

The structural and chemical information for pristine AuCu bimetallic NPs is displayed in Fig. 1a–f. Well-dispersed 10.27 ($\pm$ 0.59) nm of pristine AuCu bimetallic NPs were successfully prepared in Fig. 1a and b. The lattice spacing of 0.205 nm and its fast Fourier transform (FFT) pattern of Au–Cu bimetallic NP are consistent with typical (020) and

($\bar{2}$00) planes of reference Au [gold; cubic, Fm-3 m(225), JCPDS #01–1172]. To identify the distribution of elements, the high-angle annular dark field scanning TEM (HAADF-STEM) and EDS elemental mapping images are shown in Fig. 1c–f. It can be confirmed that Au and Cu are distributed in the AuCu bimetallic NP. By the EDS elemental mapping and inductively coupled plasma mass spectroscopy (ICP-MS) analysis, the Au to Cu atomic ratio is 71.0–29.0 and 76.8–23.2, respectively, in Table S1. On average, the atomic ratio of Au is clearly much higher than Cu. Monometallic Au and Cu NPs were also prepared in Fig. S1. About 10 nm of Au and Cu NPs were synthesized, and their lattice spacing is well-matched with (111) plane of reference Au and Cu [copper; cubic, Fm-3 m(225), JCPDS #01–1241], respectively. Additional microstructures of Au, pristine AuCu and Cu NPs were investigated by X-ray diffractometer (XRD) analysis (Fig. S2a). The Au and pristine AuCu NPs show typical diffraction patterns of the reference Au, including (111) and (200) planes and no impurities (*e.g.*, Cu, CuO, and Cu$_2$O). In particular, the peak shift of pristine AuCu NPs indicates that part of the gold is replaced by Cu atoms while maintaining the cubic crystal structure, resulting in a decrease of lattice parameter [43]. The lattice parameter (a = 0.398 nm) of pristine AuCu NPs is obtained from d < 111 > value (d <111 > = 2.30 Å; from 2θ = 39.07°) using the modified Vegard's law [44], which corresponds to the peak shift for specific alloy composition (Au:Cu = 0.75:0.25) [45]. In addition, an intermetallic AuCu nanocrystal (ordered alloy) generally shows super-lattice reflections of 110 [46,47]. However, the absence of the peak corresponding to the (110) plane on the pristine AuCu NPs indicates that the pristine AuCu is formed as a random alloy. The diffraction pattern of
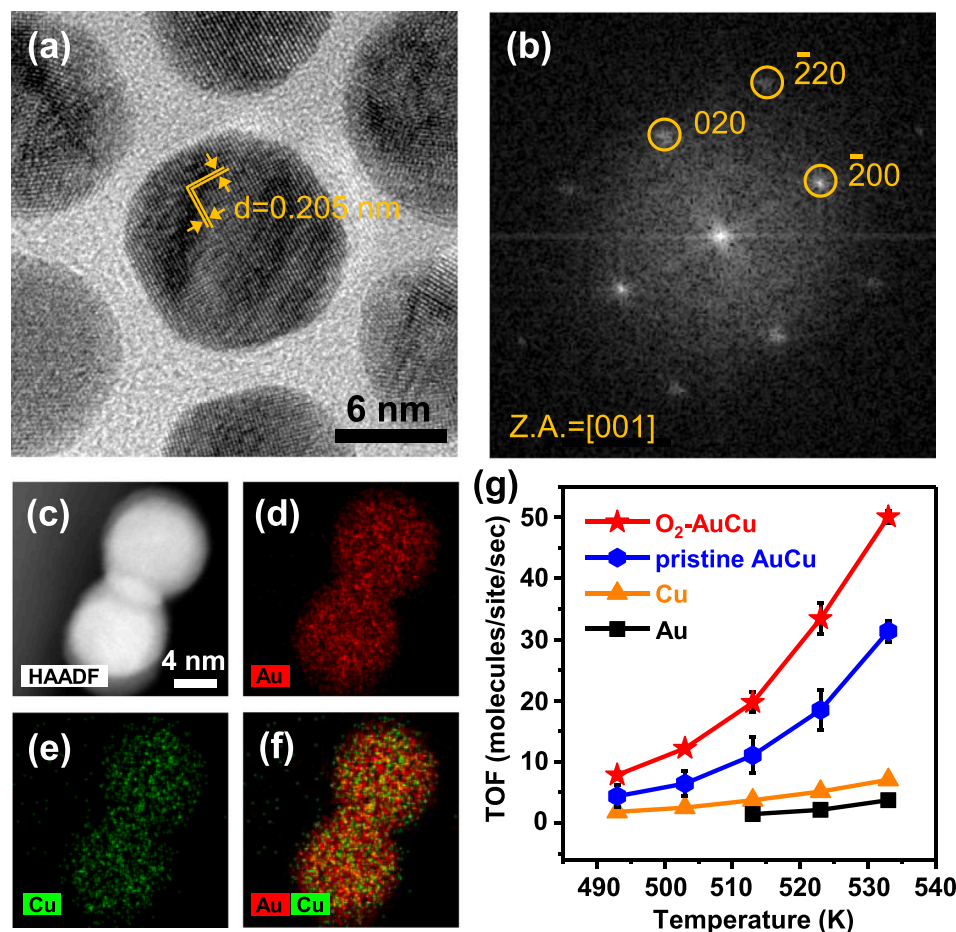

Fig. 1. Representative (a) TEM image and (b) corresponding fast Fourier-transform (FFT) patterns of AuCu NPs. Representative (c) HAADF-STEM and elemental mapping images for (d) Au, (e) Cu, and (f) overlapping elements. (g) Catalytic performance for CO oxidation of O$_2$-AuCu, AuCu, Cu, and Au nanocatalysts on SiO$_2$ substrate (reaction condition: CO+O$_2$; 1:2.5, balancing gas: He).

Cu NPs is well-matched with metallic Cu with a trace of Cu₂O [cuprous oxide; cubic, Pn-3 m(224), JCPDS #05–0667], which is a common phenomenon in the synthesis of Cu NPs [48]. In this work, we assume that the topmost surface of metallic Cu exposed in air conditions is mainly composed of Cu₂O species. Along with XRD analysis, we can also confirm the alloy *via* plasmon excitation of Au and Cu NPs in the visible region. The plasmon absorption of Au and Cu are observed at 520 and 600 nm in UV–vis spectra, respectively (Fig. S2b). On the other hand, the plasmonic peak of AuCu NPs shows more redshift (at 534 nm) than monometallic Au, which indicates the formation of Au–Cu alloy [43].

3.2. Catalytic performance

As we mentioned about bimetallic synergy in the Introduction, the oxidation reaction induces atomic restructuring in the bimetallic nanocrystals, which produces a metal–metal oxide interface showing significantly enhanced catalytic kinetics for CO oxidation [9,10,49]. To figure out the bimetallic synergy of the AuCu nanocatalyst on the silica substrate, we prepared an O₂ pretreated AuCu nanocatalyst at 573 K, hereafter referred to as the O₂-AuCu nanocatalyst. The samples for the catalytic performance test were prepared using a spin coater (Fig. S3), and catalytic activity was measured under a CO/O₂ gas mixture (1:2.5, CO oxidation environment) in Fig. 1g. The O₂-AuCu nanocatalyst shows superior catalytic performance to the pristine AuCu, Cu, and Au nanocatalysts, indicating that the O₂ pretreatment is an effective way to enhance the catalytic activity of the AuCu catalyst. A similar trend with the oxidation effect on AuCu NPs is also confirmed by comparing TOF values for the first and second cycles of the pristine AuCu catalyst in Fig. S4a. The TOF value for the second cycle shows an enhancement of catalytic activity over that of the first cycle, which might indicate that the CO oxidation environment (CO/O₂ = 1:2.5) induced the oxidation effect on pristine AuCu NPs. Based on the catalytic investigation in Fig. S4a, activation energies for the first and second cycles of the pristine AuCu nanocatalyst are calculated as 26.04 and 19.90 kcal/mol, respectively, which also indicates that the pristine AuCu nanocatalyst becomes more catalytically active after the CO oxidation reaction in Fig. S4b. The catalytic activation of the pristine AuCu catalyst during the CO oxidation is intensively discussed in Section 3.5. The oxidation of the AuCu catalyst successfully advances its catalytic performance for the CO oxidation reaction. We carried out sophisticated real-time surface
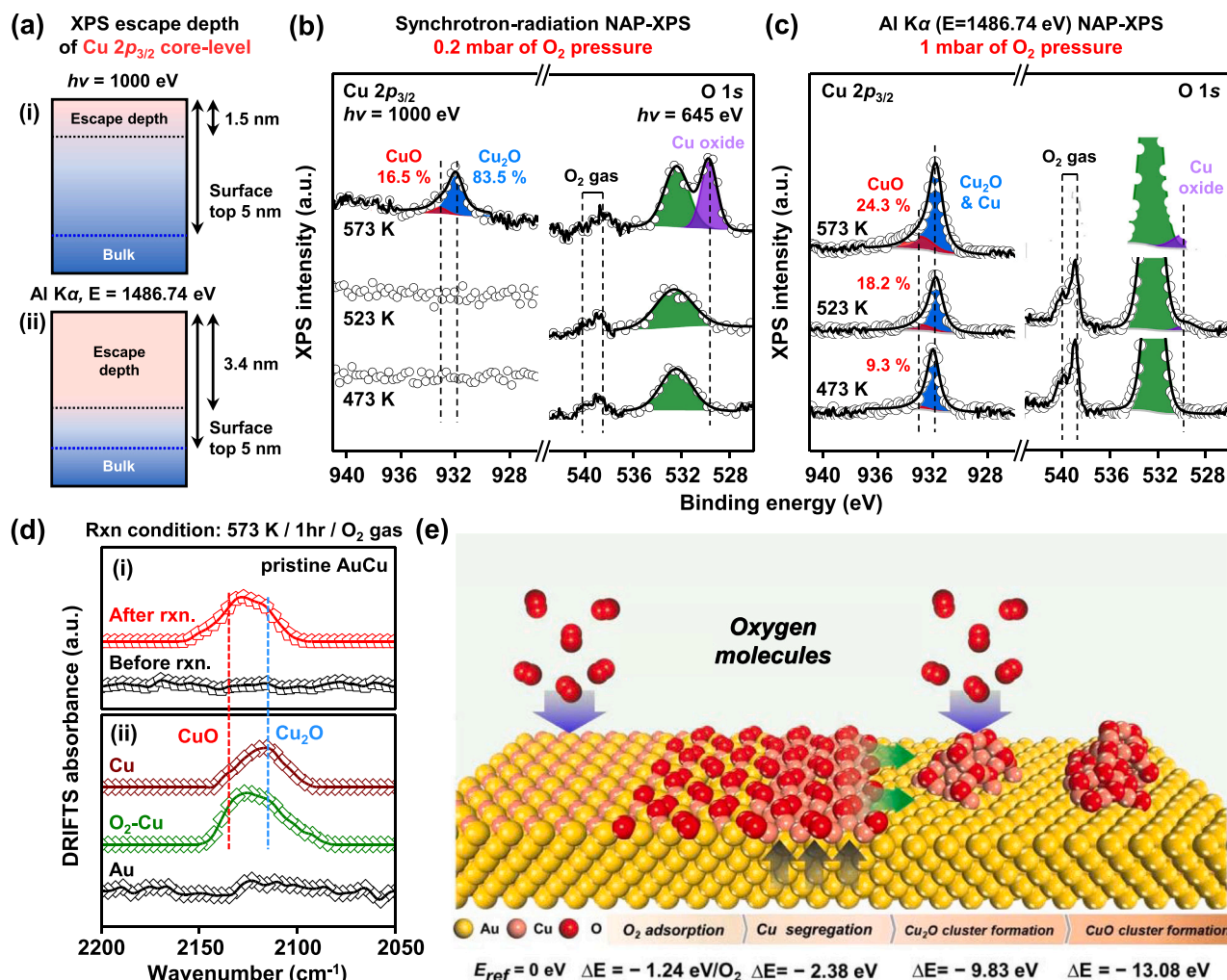

Fig. 2. (a) XPS escape depth for Cu $2p_{2/3}$ core-level spectra from (i) synchrotron-radiation NAP-XPS and (ii) Al Kα (E = 1486.74 eV) NAP-XPS measurements. The XPS escape depth is three times the electron inelastic mean free paths (~95% of the signal). (b) Synchrotron-radiation NAP-XPS measurements for (left) Cu $2p_{3/2}$ (hν = 1000 eV) and (right) O 1s (hν = 645 eV) core-level spectra under 0.2 mbar of O₂ pressure at elevated temperature. (c) Al Kα (E = 1486.74 eV) NAP-XPS measurements for (left) Cu $2p_{3/2}$ and (right) O 1s core-level spectra under 1 mbar of O₂ pressure at elevated temperature. (d) DRIFT spectra for CO adsorption of AuCu catalyst (i) before and after oxidation reaction under O₂ gas at 573 K, and spectra (ii) of CO adsorption of O₂-Cu, Cu, and Au catalysts. (e) Schematic model of sequential Cu₂O and CuO formation. The ΔE presents the DFT-calculated reaction energy associated with the corresponding elemental process. The ΔE of Cu surface segregation and Cu₂O and CuO formation was calculated by adding the stoichiometric quantity of gas phase oxygen molecules to the system. The sequential exothermic ΔE values confirm that formation of CuO on Au is thermodynamically driven.

analysis under oxidation reaction conditions to unveil the physical and chemical changes on the surface of AuCu NP.

3.3. Atomic restructuring of AuCu nanocrystals

To gain insight into the chemical changes Cu and O species undergo in AuCu NPs during the oxidation reaction, the NAP-XPS analysis of pristine AuCu NPs on SiO$_2$ substrate is investigated at elevated temperatures under O$_2$ gas (Fig. 2a–c). To observe sophisticated chemical changes of Cu and O species on the surface, we controlled the electron-escape depth in XPS measurements by changing the photon energy using synchrotron radiation and an Al Kα (E = 1486.74 eV) as an X-ray source in Fig. 2a [50]. The incident photon energies of each obtained Cu 2p and O 1s core-level spectrum are adjusted to 1000 and 645 eV for collecting escaping photoelectrons from the topmost surface (*i.e.,* kinetic energy $\cong$ 100 eV; escape depth = ~1.5 nm; ~95% of the signal; Fig. 2a-(i)) of pristine AuCu NPs in Fig. 2b. Under 523 K, there is no peak of copper species in the Cu 2$p_{3/2}$ core-level XPS region (*i.e.,* Au atoms are relatively dominant near the top surface), as shown on the left side of Fig. 2b. However, a distinct peak can be confirmed from 573 K, which indicates that the copper atoms inside the pristine AuCu NP are segregated to the topmost surface. The distinct peak can be deconvoluted into 83.5% of Cu/Cu$_2$O (Cu or Cu$_2$O; blue, 931.9 eV) and 16.5% of CuO (red, 933.1 eV) with a difference of 1.2 eV [51]. Likewise, from the O 1s core-level spectra on the right side of Fig. 2b, there are only three peaks relevant to gas (two peaks at around 539 eV) and lattice oxygen in the SiO$_2$ substrate (green peak, 532.6 eV) for XPS specimen under 523 K. The strong copper oxide peak (purple, 529.8 eV) appears at 573 K. The chemical states of the blue peak in Cu 2$p_{3/2}$ core-level spectrum are metallic Cu and Cu$_2$O, showing a similar position at 931.9 eV. It is difficult to distinguish either metallic Cu or Cu$_2$O from this peak. However, it can be detected from the presence of the strong copper oxide peak at 573 K in the O 1s core-level spectrum (right side of Fig. 2b), which means that the Cu$_2$O is a dominant state in the blue peak (left side of Fig. 2b). We also note that Au oxidation states do not change during the oxidation reaction, as shown in Fig. S5.

For a comprehensive understanding of the chemical change, analysis of NAP-XPS with Al Kα (E = 1486.74 eV; escape depth = ~3.5 nm; ~95% of the signal; Fig. 2a-(ii)) was also carried out under 1 mbar of O$_2$ gas, as shown in Fig. 2c. Unlike the results *via* the synchrotron-radiation, the Al Kα NAP-XPS signal of the Cu/Cu$_2$O species inside the NPs could be confirmed at temperatures below 573 K, which means that AuCu NPs exist as an alloy. As the temperature increased up to 573 K under higher O$_2$ gas pressures than that of synchrotron-radiation (Fig. 2b), the phase transformation of Cu/Cu$_2$O into the CuO state was mainly confirmed in the left side of Fig. 2c, which can be rationalized by the formation of a copper oxide peak by O 1s core-level spectrum on the right side of Fig. 2c.

The formation of copper oxides on the AuCu nanocrystals driven from the atomic restructuring can be explained by the CO adsorption test using a DRIFTS investigation in Fig. 2d. The CO adsorption analysis also delivers important insights relevant to the active site in CO oxidation reaction, because it is the first step in the reaction, regardless of the catalytic mechanism. Plots for CO adsorption of the pristine AuCu/SiO$_2$ nanocatalyst before and after oxidation reaction are displayed in Fig. 2d-(i); those of reference samples are displayed in Fig. 2d-(ii). To assign a position of CO adsorption to correspond with Cu/Cu$_2$O or CuO, we prepared the reference samples, which mainly offer Cu/Cu$_2$O (Cu/SiO$_2$ nanocatalyst) and CuO (O$_2$-Cu/SiO$_2$ nanocatalyst; O$_2$-pretreated Cu NPs for 1 hr at 573 K) states on the surface, as shown in Fig. S6. From Fig. 2d-(ii), the spectrum of both Cu/SiO$_2$ and O$_2$-Cu/SiO$_2$ nanocatalysts commonly shows the mixture of two peaks at 2114 and 2135 cm^{-1}, and the peak at 2135 cm^{-1} is mainly observed over the O$_2$-Cu/SiO$_2$ nanocatalyst (*i.e.,* CuO state). The CO adsorption peak at 2114 cm^{-1} is assigned to a carbonyl species on Cu$_2$O (Cu$^+$) NPs [52,53], and the peak at 2135 cm^{-1} indicates a CO stretching vibration on CuO (Cu^{2+}) species

[54,55]. There is no CO adsorption peak in the spectrum of the Au/SiO$_2$ nanocatalyst. By comparing with reference data in Fig. 2d-(ii), we can interpret the significant change between before and after reaction spectra of the pristine AuCu/SiO$_2$ nanocatalyst in Fig. 2d-(i). Before the reaction, the CO adsorption peak is absent in the spectrum of the pristine AuCu/SiO$_2$ nanocatalyst, which resembles the Au/SiO$_2$ nanocatalyst and is well-matched with the results (*i.e.,* Au dominant surface of pristine AuCu NPs before the reaction) from NAP-XPS in Fig. 2b and c. On the other hand, two peaks appear at 2135 and 2114 cm^{-1} after the reaction. This result suggests that the CuO species are dominantly formed on the surface after the oxidation reaction. The formed CuO mainly acts as an active site over the O$_2$-AuCu/SiO$_2$ catalyst for CO oxidation reaction, as compared to Fig. 2d-(ii). It can be confirmed by comparing the catalytic activity for CO oxidation on the O$_2$-AuCu/SiO$_2$ and the spent AuCu/SiO$_2$ (after 1st catalytic cycle of the pristine AuCu/SiO$_2$ in Fig. S4) samples, as shown in Fig. S7. The O$_2$-AuCu/SiO$_2$ nanocatalyst shows more active catalytic performance than the spent AuCu/SiO$_2$ nanocatalyst. The results can be explained by *ex situ* XPS characterization in Fig. S8. Both O$_2$-AuCu and spent AuCu samples show the similar oxidation state of Au, but it is easily confirmed that the O$_2$-AuCu sample was much more oxidized (*i.e.,* CuO species is dominant) than the spent AuCu sample (*i.e.,* CuO/Cu$_2$O mixture; CuO$_x$). Thus, it is believed that the dominant CuO species shows more catalytic activity than the CuO/Cu$_2$O mixture at interface with Au. From the two powerful *in situ* surface techniques (NAP-XPS and DRIFTS), we experimentally clarified the surface restructuring and formation mechanism of CuO *via* Cu$_2$O species on the NP surface during the oxidation reaction. These experimental results are also rationalized by DFT calculation in terms of thermodynamics.

We studied the sequential process of initial segregation of Cu and subsequent formation of CuO$_x$ with a DFT-constructed Au$_3$Cu (100) slab model under oxidative conditions. The details of the DFT calculation method and the morphology of the DFT-constructed models are presented in chapter 2.7 and chapter 3.5, respectively. The DFT-calculated overall energetics of the oxygen-driven surface segregation of Cu atoms represent that the formation process of Cu$_2$O (Cu$_{32}$O$_{16}$) cluster on an Au surface is thermodynamically feasible (Fig. 2e). All Cu atoms segregated to the surface were extracted from the upper four layers of the six-layered Au$_3$Cu slab model (Fig. S9), transforming them into a Cu$_2$O cluster. Interestingly, the further transformation of Cu$_2$O to CuO (Cu$_{32}$O$_{32}$) was strongly thermodynamically-driven, confirming our experimental finding that Cu$_2$O was transformed to CuO under oxidative conditions (Fig. 2b and c). The relative energetic location of each state presented in Fig. 2e is displayed in Fig. S10.

3.4. Direct observation for a formation of CuO$_x$–Au interface

With the *operando* spectroscopic analysis and DFT calculation regarding the formation of CuO$_x$ species on the surface, we also studied the real-time morphological change of pristine AuCu NP using an aberration-corrected E-TEM. The real-time chemical interaction between AuCu NP and O$_2$ molecules is introduced in Video S1. For capturing the situation for atomic restructuring, the amorphous capping layer was minimized before the reaction (see chapter 2.6). The Video S1 involves the following two steps: (i) formation of metastable Cu$_2$O clusters, and (ii) crystallization of Cu$_2$O clusters. For detailed information on the atomic restructuring phenomenon, the E-TEM images of pristine AuCu NP are displayed in Fig. 3. Before the reaction, the pristine AuCu NP exhibits spherical morphology with a limited amorphous capping layer (Fig. 3a). After the O$_2$ gas fills up to 0.1 mbar at RT, the amorphous capping layer is instantaneously removed, and a Cu$_2$O cluster with a lattice spacing of 0.246 nm is formed on the Au–Cu NP surface by Cu segregation, consistent with typical (111) plane of reference Cu$_2$O in Fig. 3b. It can be confirmed that the formed heterostructure of Cu$_2$O/Au–Cu NP follows the results of DFT calculation about Cu$_2$O cluster formation on the surface (Fig. 2e). Furthermore, it was

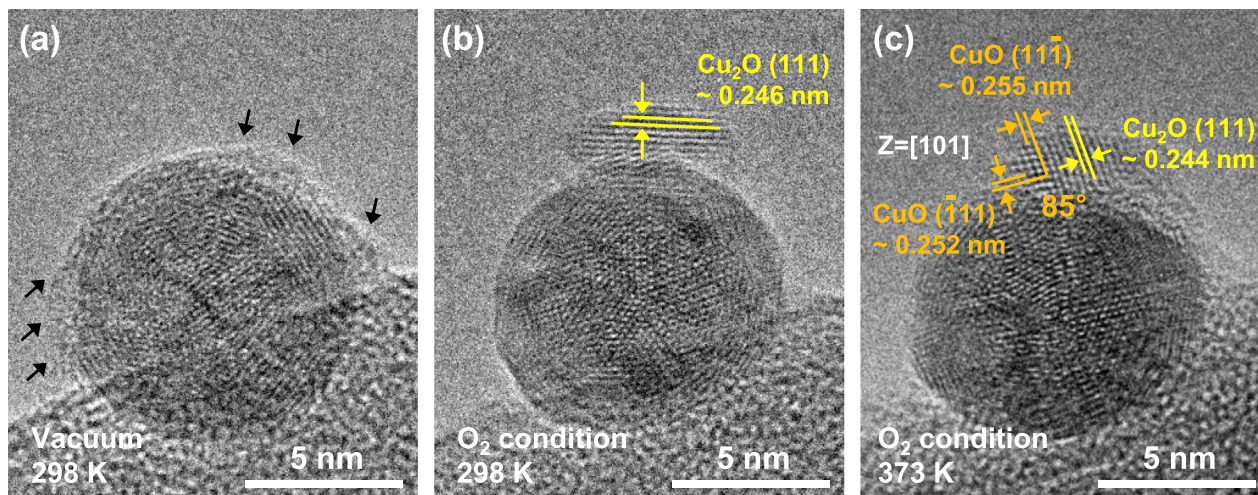## E-TEM observation under 0.1 mbar of O_2 gas

Fig. 3. E-TEM images for the AuCu NP in the vacuum at (a) RT, and under 0.1 mbar of O_2 gas at (b) RT, and (c) 373 K. Black arrows: an amorphous carbonaceous layer from capping agent.

reported that the Cu atoms prefer the (010) plane for segregation to form Cu_2O on the AuCu surface in the AuCu/CeO_2 model system [21]. As the temperature increased up to 373 K, the CuO phase was created by the transformation of a Cu_2O cluster with lattice spacing of 0.255 and 0.252 nm with 85° between the two crystal planes, which are in agreement with typical ($\bar{1}11$) and ($11\bar{1}$) planes of reference CuO [cupric oxide; monoclinic, C2/c(15), JCPDS #41–0254], as shown in Fig. 3c. The Au–Cu NP gets smaller and flattens as the Cu atoms segregate toward the surface. At 423 K, the CuO phase is dominant in the cluster, indicating the formation of CuO_x/Au heterostructure, as shown in Fig. S11. The *ex situ* TEM images for CuO_x/Au heterostructure (after the reaction at 573 K) are also obtained in Fig. S12. From the XRD analysis in Fig. S13, the peak shift to the left side (*i.e.*, to a low degree) of O_2-AuCu NPs means that the dealloying of some Cu with Au atoms occurred, which is also indirect evidence of atomic restructuring. Therefore, we can successfully observe the dynamic morphological change, resulting in capturing the formation of oxygen-driven CuO_x/Au heterostructure.

3.5. Catalytic role of the CuOx–Au interface

To unveil a correlation between the formation of CuO_x–Au interface and reactivity for CO oxidation, an *operando* NAP-XPS investigation and DFT calculation were performed in Fig. 4. The *operando* NAP-XPS measurement with Al $K\alpha$ over the pristine AuCu/SiO_2 nanocatalyst was carried out in a 0.4 mbar CO and 1.0 mbar O_2 gas mixture (1:2.5 ratio). Mass spectrometric intensities of O_2 ($m/z = 32$), CO ($m/z = 40$), and CO_2 ($m/z = 44$) were recorded during the NAP-XPS measurement in Fig. 4a. There is generally a non-linear relationship between the temperature and CO catalytic conversion, as exemplified by a trend of temperature-dependent catalytic activity for CO oxidation over the Au/SiO_2 nanocatalyst. (Fig. S14). However, the CO_2 production of the AuCu/SiO_2 nanocatalyst does not follow the general trend, like that of the Au/SiO_2 nanocatalyst; see the rise of CO_2 production over AuCu and Au/SiO_2 nanocatalysts between elevated temperatures from 473 to 523–573 K. The CO conversion of the AuCu/SiO_2 nanocatalyst at 473 and 523 K (black arrows) is drastic compared to the CO conversion trend of the Au/SiO_2 catalyst, indicating that the chemical changes in the AuCu/SiO_2 nanocatalyst occurred from 473 K. The chemical changes from 473 K can be elucidated by results of NAP-XPS measurement for Cu $2p_{3/2}$ core-level (Fig. 4b) and Cu LMM auger (Fig. 4c) spectra with Au 4f core-level spectrum (Fig. S15). The plot for a Cu $2p_{3/2}$/Au 4f area ratio

is employed to explain the atomic restructuring near the surface, as shown in Fig. S16. The percentage value is for comparing the relative portion of surface Cu species, and the results show that Cu segregation occurred from 473 to 573 K.

In addition, the Cu oxidation states during CO oxidation are analyzed by the results of the Cu LMM auger spectra [56]. Metallic Cu (kinetic energy = 918.6 eV) is the dominant state on the AuCu/SiO_2 catalyst at 423 K, which shows increased Cu_2O (kinetic energy = 916.8 eV) from 473 K to 523 K; the Cu_2O transforms into CuO (kinetic energy = 917.7 eV) as the temperature reaches 573 K. Although the low signal-to-noise ratio (SNR) at 473 K is not favorable enough to assign the Cu oxidation states, the temperature-dependent trends for Cu oxidation states during the CO oxidation can be demonstrated roughly *via* Cu LMM auger spectra in a temperature range from 423 to 573 K. This tendency is similar to results from the *in situ* NAP-XPS analysis during the oxidation reaction for an oxygen-driven atomic restructuring of AuCu NPs in Fig. 2. Like the result of Au 4f core-level during the oxidation reaction in Fig. S5, Au oxidation states do not change during the CO oxidation reaction in Fig. S15. Also, the formation of oxygen-driven heterostructure with CuO_x-Au interface is confirmed by EDS mapping investigation of AuCu/SiO_2 nanocatalyst after the CO oxidation reaction, even though the sintering of particles occurs in Fig. S17. Therefore, we confirmed that the formation of CuO_x-Au interface boosts catalytic activity during CO oxidation.

To understand the catalytic energy requirements at the CuO–Au interface, we performed a DFT calculation using a confined model structure of CuO slab ($Cu_{70}O_{70}$) on Au(100) to study the mechanism of CO oxidation at the interfaces in Fig. S18. The interface between metal NPs and supporting oxides has been recognized as a reaction site for interface-mediated oxidation reactions. Moreover, electronic interactions between supported metal NPs and supporting oxides (and *vice versa*) sometimes modify the chemical activity of the interfacial oxygen ions [41,42]. Previously, we found that the oxygen vacancy formation energy, E_{vac}, of a CeO_2 cluster supported on a Au(111) substrate was significantly reduced from the original E_{vac} of CeO_2(111) [57]. A similar trend was observed in our CuO/Au(100) system as the E_{vac} of CuO(111) ($E_{vac} = 2.00$ eV) was reduced to 0.33 eV, as shown in Fig. S19. Because this calculated E_{vac} is almost identical to the absolute value of the entropic contribution to the Gibbs free energy of CO adsorption (TΔS) at standard conditions [57], the CuO NP formed on Au NP is highly likely to be rich in oxygen vacancies. The Bader charge analysis results show that the Cu layer at the interface between CuO and Au draws electrons
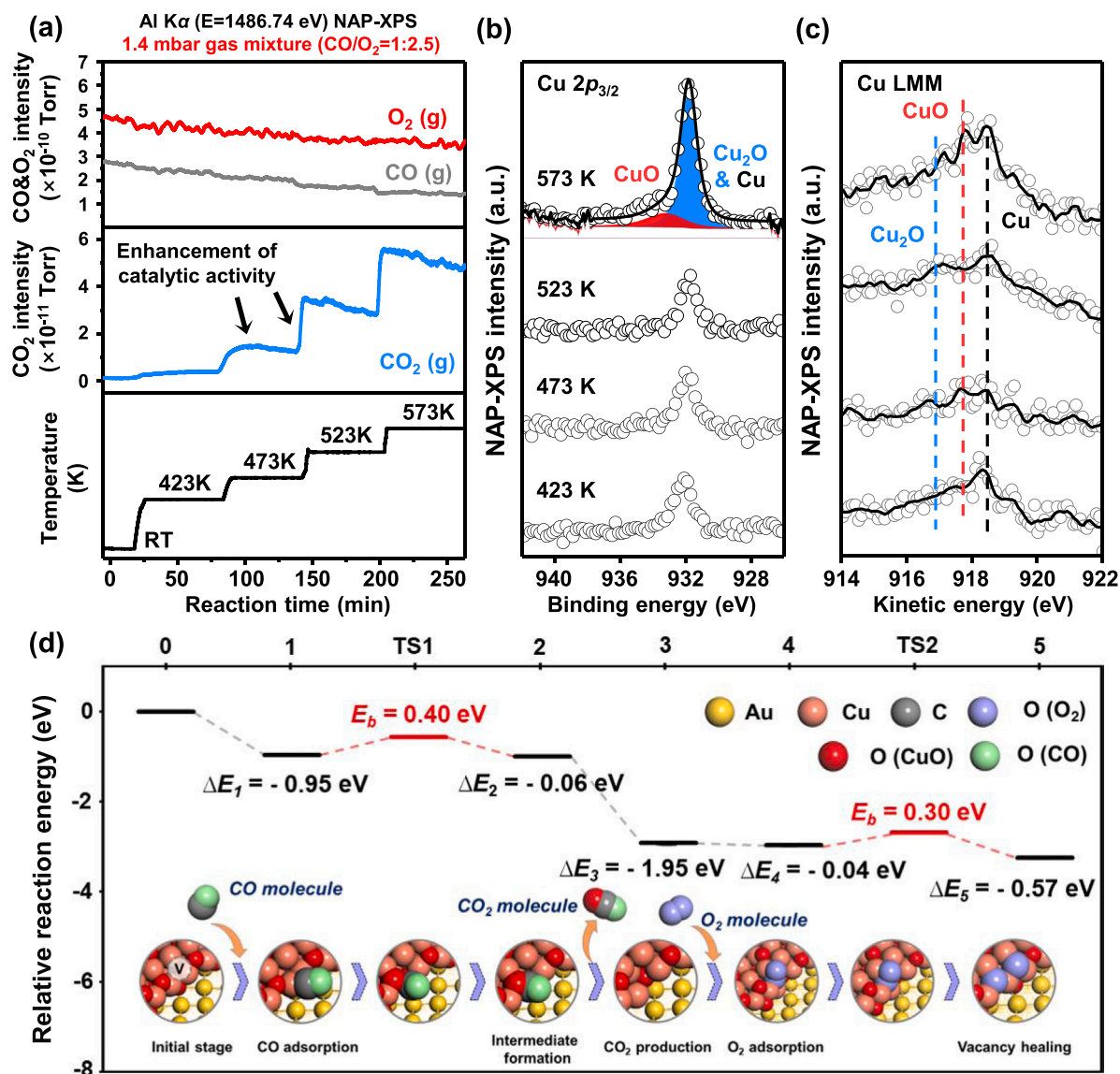
Fig. 4. Mass spectrometry profile and *operando* NAP-XPS measurements with Al Kα (E = 1486.74 eV) of the pristine AuCu/SiO$_2$ nanocatalyst under 0.4 mbar CO and 1.0 mbar O$_2$ mixed gas (1:2.5 ratio). (a) Mass spectrometric data for CO oxidation; m/z = 28 (CO; gray), m/z = 32 (O$_2$; red), m/z = 44 (CO$_2$; blue), and temperature profiles at RT, 423, 473, 523, and 573 K. *Operando* NAP-XPS measurements for (b) Cu 2$p_{3/2}$ core-level and (c) Cu LMM auger spectra under 1.4 mbar of reactant gas mixture (CO/O$_2$ =1:2.5) at elevated temperature. (d) Reaction pathway of CO oxidation at the CuO-Au interface through the Mars-van Krevelen mechanism. The DE$_n$ presents the reaction energy calculated by DE$_n$ = E_n − E_{n-1}. Overall reaction steps are energetic with low energy barrier, E_b of 0.40 eV. The highlighted white circle in the initial stage denotes the location of the pre-existing oxygen vacancy.

from the Au substrate, being rich in electrons and more easily releasing oxygen ions. Notably, the calculated weak initial CO binding energy, E_{bind}, of the CuO slab of CuO/Au (E_{bind} = −0.34 eV) was increased to − 0.95 eV upon introduction of an oxygen vacancy, supporting our DRIFTS results that the CO is mainly bound and activated by CuO (Fig. 2d). The formation of oxygen vacancies is experimentally investigated by EPR analysis, as shown in Fig. S20. It is possible to do qualitative analysis for oxygen vacancy by comparing the EPR signal on each specimen with a g-factor of ~2.004 by trapping electrons at an oxygen vacancy site [58–60]. The EPR spectrum of the AuCu/SiO$_2$ nanocatalyst only shows a signal with a g-factor of 2.933 and no signal with a g-factor of 2.004. On the other hand, the EPR spectrum of O$_2$-AuCu/SiO$_2$ nanocatalyst shows strong EPR signals with g-factors of 2.059 and 2.006, which means that the O$_2$-AuCu/SiO$_2$ nanocatalyst includes the oxygen vacancy. The signal with a g-factor of 2.933 in the AuCu/SiO$_2$ nanocatalyst was not resolved, and we think that the signal comes from Au species [61]. It is considered that the signal with a g-factor of 2.933 is

also included in the broad and asymmetric EPR spectrum of the O$_2$-AuCu/SiO$_2$ nanocatalyst. The strong signal with a g-factor of 2.059 indicates the Cu^{2+} species [60,62], which implies oxygen-driven Cu segregation in the O$_2$-AuCu/SiO$_2$ nanocatalyst. Therefore, we confirmed the oxygen-driven Cu segregation, and the EPR investigation confirmed the presence of oxygen vacancy in the O$_2$-AuCu/SiO$_2$ nanocatalyst.

The overall CO oxidation pathway and the corresponding energetics presented in Fig. 4d show that the vacated CuO$_x$/Au is reactive for CO oxidation through the interface-mediated Mars-van Krevelen (MvK) mechanism. Formation and production of CO$_2$ from a CuO$_x$-bound CO requires only 0.4 eV of the energy barrier, E_b, confirming that this process is facile. We note that the E_b of 0.4 eV was calculated in the presence of a pre-formed oxygen vacancy by generating a bent CO$_2$-like intermediate using another adjacent oxygen ion of CuO$_x$. Two adjacent oxygen vacancies were replenished by an O$_2$ molecule through stages 3 and 4 (Fig. 4d) to calculate the ΔE of oxygen vacancy healing, which evaluates the oxygen affinity of the catalyst model; however, oxygen

vacancies can be spontaneously generated at the CuO/Au interface, due to the modified electronic structure of the Cu ions at the interface. Based on recent consecutive findings that the E_{vac} scales the catalytic activity of the metal–oxide interfaces toward oxidation reactions [57,63,64], the low E_{vac} of 0.33 eV of the CuO/Au interface naturally implies the high catalytic activity of our CuO_x/Au catalyst for CO oxidation. The results of theoretical calculation for the catalytic mechanism can be supported by experimental study for CO dependency on the catalytic activity of the O_2-AuCu, as shown in Fig. S21. The study of CO dependency is one of the ways to figure out the catalytic mechanism for CO oxidation. The O_2-AuCu nanocatalyst shows a negative slope under a low CO pressure region, indicating that the reactive surface sites of the O_2-AuCu nanocatalyst are continuously being filled and blocked by CO adsorption. In the high CO pressure region, the O_2-AuCu nanocatalyst shows the near-zero slope maintaining the CO oxidation reaction, which means that the reaction can progress, even if the active surface sites are fully saturated by CO adsorption. These results suggest that the O_2-AuCu nanocatalyst may follow the MvK mechanism [65,66].

4. Conclusion

Using silica–supported AuCu nanocatalysts for CO oxidation as a model catalyst, we demonstrate the formation mechanism of heterostructure with metal–metal oxide interface in an Au–Cu bimetal system under O_2 and CO oxidation conditions at ambient pressure, which drives the catalytic synergy for the CO oxidation reaction. The oxygen pretreated AuCu/SiO$_2$ nanocatalysts shows significantly enhanced catalytic performance, which is ascribed to the formation of CuO_x/Au interfacial sites, including oxygen vacancy. Formation of CuO clusters *via* Cu$_2$O on the surface of AuCu NP by atomic restructuring during oxidation reaction was unraveled by combined *in situ* measurements (*e.g.,* NAP-XPS, DRIFTS, and E-TEM) and DFT calculation. In addition, the *operando* NAP-XPS analysis and DFT calculation suggest the active sites and catalytic mechanism: the CuO_x/Au interface with oxygen vacancies acts as an active site, facilitating the effective CO conversion perhaps *via* MvK mechanism. Our results unveiled a direct correlation between evolution of the CuO_x/Au interfacial sites and its catalysis for CO oxidation, similar to the EMSI effect, which was difficult to establish in previous *ex situ* experiments. The insights for catalysis over the AuCu/SiO$_2$ nanocatalyst provide a different perspective for understanding the EMSI effect on Au-based mixed catalysis and serve potential applications for rational bimetal nanocatalysts design.

CRediT authorship contribution statement

Taek-Seung Kim: Conceptualization, Data processing, Formal analysis, Investigation, Writing – original draft. **Hyuk Choi**: DFT calculation, Writing – original draft, Methodology. **Daeho Kim**: Formal analysis. **Hee Chan Song**: Formal analysis. **Yusik Oh**: Validation. **Beomgyun Jeong**: Formal analysis, Resources, Validation. **Jouhahn Lee**: Resources. **Ki-Jeong Kim**: Resources. **Jae Won Shin**: Formal analysis, Investigation, Resources, Validation. **Hye Ryung Byon**: Validation. **Ryong Ryoo**: Resources, Validation. **Hyun You Kim**: Supervision, Writing – review & editing. **Jeong Young Park**: Supervision, Writing – review & editing.

Declaration of Competing Interest

The authors declare that they have no known competing financial interests or personal relationships that could have appeared to influence the work reported in this paper.

Data availability

Data will be made available on request.

Appendix A. Supporting information

Supplementary data associated with this article can be found in the online version at doi:10.1016/j.apcatb.2023.122704.

References

1 R.M. Heck, R.J. Farrauto, Automobile exhaust catalysts, Appl. Catal. A Gen. 221 (2001) 443–457, https://doi.org/10.1016/S0926-860X(01)00818-3.

2 G. Pattrick, E. van der Lingen, C.W. Corti, R.J. Holliday, D.T. Thompson, The potential for use of gold in automotive pollution control technologies: a short review, Top. Catal. 30 (2004) 273–279, https://doi.org/10.1023/B:TOCA.0000029762.14168.d8.

3 O. Pozdnyakova, D. Teschner, A. Wootsch, J. Kröhnert, H. Steinhauer, H. Sauer, L. Toth, F.C. Jentoft, A. Knop-Gericke, Z. Paál, R. Schlögl, Preferential CO oxidation in hydrogen (PROX) on ceria-supported catalysts, part I: Oxidation state and surface species on Pt/CeO$_2$ under reaction conditions, J. Catal. 237 (2006) 1–16, https://doi.org/10.1016/j.jcat.2005.10.014.

4 M.A. Van Spronsen, J.W.M. Frenken, I.M.N. Groot, Surface science under reaction condition: CO oxidation on Pt and Pd model catalysts, Chem. Soc. Rev. 46 (2017) 4347–4374, https://doi.org/10.1039/C7CS00045F.

5 H.-J. Freund, G. Meijer, M. Scheffler, R. Schlögl, M. Wolf, CO oxidation as a prototypical reaction for heterogeneous processes, Angew. Chem. Int. Ed. 50 (2011) 10064–10094, https://doi.org/10.1002/anie.201101378.

6 G. Ertl, Oscillatory kinetics and spatio-temporal self-organization in reactions at solid surfaces, Science 254 (1991) 1750–1755, https://doi.org/10.1126/science.254.5039.1750.

7 T. Gritsch, D. Coulman, R.J. Behm, G. Ertl, Mechanism of the CO-induced $1 \times 2 \rightarrow 1 \times 1$ structural transformation of Pt(110), Phys. Rev. Lett. 63 (1989) 1086–1089, https://doi.org/10.1103/PhysRevLett.63.1086.

8 M.J. Kale, P. Christopher, Utilizing quantitative in situ FTIR spectroscopy to identify well-coordinated Pt atoms as the active site for CO oxidation on Al2O3-supported Pt catalysts, ACS Catal. 6 (2016) 5599–5609, https://doi.org/10.1021/acscatal.6b01128.

9 C.H. Wu, C. Liu, D. Su, H.L. Xin, H.-T. Fang, B. Eren, S. Zhang, C.B. Murray, M. B. Salmeron, Bimetallic synergy in cobalt–palladium nanocatalysts for CO oxidation, Nat. Catal. 2 (2018) 78–85, https://doi.org/10.1038/s41929-018-0190-6.

10 T.-S. Kim, J. Kim, H.C. Song, D. Kim, B. Jeong, J. Lee, J.W. Shin, R. Ryoo, J.Y. Park, Catalytic synergy on PtNi bimetal catalysts driven by interfacial intermediate structures, ACS Catal. 10 (2020) 10459–10467, https://doi.org/10.1021/acscatal.0c02467.

11 M. Ahmadi, F. Behafarid, C. Cui, P. Strasser, B.R. Cuenya, Long-range segregation phenomena in shape-selected bimetallic nanoparticles: chemical state effects, ACS Nano 7 (2013) 9195–9204, https://doi.org/10.1021/nn403793a.

12 H. Liao, A. Fisher, Z.J. Xu, Surface segregation in bimetallic nanoparticles: a critical issue in electrocatalyst engineering, Small 11 (2015) 3221–3246, https://doi.org/10.1002/smll.201403380.

13 E.K. Gibson, A.M. Beale, C.R.A. Catlow, A. Chutia, D. Gianolio, A. Gould, A. Kroner, K.M.H. Mohammed, M. Perdjon, S.M. Roger, P.P. Wells, Restructuring of AuPd nanoparticles studied by a combined XAFS/DRIFTS approach, Chem. Mater. 27 (2015) 3714–3720, https://doi.org/10.1021/acs.chemmater.5b00866.

14 S.J. Tauster, S.C. Fung, R.L. Garten, Strong metal-support interactions. Group 8 noble metals supported on titanium dioxide, J. Am. Chem. Soc. 100 (1978) 170–175, https://doi.org/10.1021/ja00469a029.

15 H. Tang, Y. Su, B. Zhang, A.F. Lee, M.A. Isaacs, K. Wilson, L. Li, Y. Ren, J. Huang, M. Haruta, B. Qiao, X. Liu, C. Jin, D. Su, J. Wang, T. Zhang, Classical strong metal–support interactions between gold nanoparticles and titanium dioxide, Sci. Adv. 3 (2017) e1700231, https://doi.org/10.1126/sciadv.1700231.

16 C.T. Campbell, Catalyst-support interactions: electronic perturbations, Nat. Chem. 4 (2012) 597–598, https://doi.org/10.1038/nchem.1412.

17 J.C. Bauer, D. Mullins, M. Li, Z. Wu, E.A. Payzant, S.H. Overbury, S. Dai, Synthesis of silica supported AuCu nanoparticle catalysts and the effects of pretreatment conditions for the CO oxidation reaction, Phys. Chem. Chem. Phys. 13 (2011) 2571–2581, https://doi.org/10.1039/C0CP01859G.

18 J.C. Bauer, G.M. Veith, L.F. Allard, Y. Oyola, S.H. Overbury, S. Dai, Silica-supported Au–CuO$_x$ hybrid nanocrystals as active and selective catalysts for the formation of acetaldehyde from the oxidation of ethanol, ACS Catal. 2 (2012) 2537–2546, https://doi.org/10.1021/cs300551r.

19 D. Kim, J. Resasco, Y. Yu, A.M. Asiri, P. Yang, Synergistic geometric and electronic effects for electrochemical reduction of carbon dioxide using gold-copper bimetallic nanoparticles, Nat. Commun. 5 (2014) 4948, https://doi.org/10.1038/ncomms5948.

20 W. Zhan, J. Wang, H. Wang, J. Zhang, X. Liu, P. Zhang, M. Chi, Y. Guo, Y. Guo, G. Lu, S. Sun, S. Dai, H. Zhu, Crystal structural effect of AuCu alloy nanoparticles on catalytic CO oxidation, J. Am. Chem. Soc. 139 (2017) 8846–8854, https://doi.org/10.1021/jacs.7b01784.

21 L. Luo, S. Chen, Q. Xu, Y. He, Z. Dong, L. Zhang, J. Zhu, Y. Du, B. Yang, C. Wang, Dynamic atom clusters on AuCu nanoparticle surface during CO oxidation, J. Am. Chem. Soc. 142 (2020) 4022–4027, https://doi.org/10.1021/jacs.9b13901.

22 E. Völker, F.J. Williams, E.J. Calvo, T. Jacob, D.J. Schiffrin, O₂ induced Cu surface segregation in Au-Cu alloys studied by angle resolved XPS and DFT modelling, Phys. Chem. Chem. Phys. 14 (2012) 7448–7455, https://doi.org/10.1039/C2CP40565B.

23 G.A. Somorjai, H. Frei, J.Y. Park, Advancing the frontiers in nanocatalysis, biointerfaces, and renewable energy conversion by innovations of surface techniques, J. Am. Chem. Soc. 131 (2009) 16589–16605, https://doi.org/10.1021/ja9061954.

24 J.I.J. Choi, T.-S. Kim, D. Kim, S.W. Lee, J.Y. Park, *Operando* surface characterization on catalytic and energy materials from single crystal to nanoparticles, ACS Nano 14 (2020) 16392–16413, https://doi.org/10.1021/acsnano.0c07549.

25 M. Chi, C. Wang, Y. Lei, G. Wang, D. Li, K.L. More, A. Lupini, L.F. Allard, N. M. Markovic, V.R. Stamenkovic, Surface faceting and elemental diffusion behaviour at atomic scale for alloy nanoparticles during *in situ* annealing, Nat. Commun. 6 (2015) 8925, https://doi.org/10.1038/ncomms9925.

26 K.-Q. Sun, S.-W. Luo, N. Xu, B.-Q. Xu, Gold nano-size effect in Au/SiO₂ for selective ethanol oxidation in aqueous solution, Catal. Lett. 124 (2008) 238–242, https://doi.org/10.1007/s10562-008-9507-4.

27 S. Oh, K. Qadir, J.Y. Park, Nature of active sites and their quantitative measurement in two-dimensional Pt metal catalysts, Catal. Lett. 147 (2016) 39–45, https://doi.org/10.1007/s10562-016-1909-0.

28 F. Zhen, S. Alayoglu, V.V. Pushkarev, S.K. Beaumont, C. Specht, F. Aksoy, Z. Liu, J. Guo, G.A. Somorjai, In situ study of oxidation states and structure of 4 nm CoPt bimetallic nanoparticles during CO oxidation using X-ray spectroscopies in comparison with reaction turnover frequency, Catal. Today 182 (2012) 54–59, https://doi.org/10.1016/j.cattod.2011.10.009.

29 G. Kim, Y. Yu, H. Lim, B. Jeong, J. Lee, J. Baik, B.S. Mun, K. Kim, AP-XPS beamline, a platform for *operando* science at Pohang Accelerator Laboratory, J. Synchrotron Radiat. 27 (2020) 507–514, https://doi.org/10.1107/S160057751901676X.

30 C. Jeong, H. Yun, H. Lee, S. Muller, J. Lee, B.S. Mun, Performance test of new near-ambient-pressure XPS at Korean Basic Science Institute and its application to CO oxidation study on Pt₃Ti polycrystalline surface, Curr. Appl. Phys. 16 (2016) 73–78, https://doi.org/10.1016/j.cap.2015.10.010.

31 W. Albrecht, A. van de Glind, H. Yoshida, Y. Isozaki, A. Imhof, A. van Blaaderen, P. E. de Jongh, K.P. de Jong, J. Zečević, S. Takeda, Impact of the electron beam on the thermal stability of gold nanorods studied by environmental transmission electron microscopy, Ultramicroscopy 193 (2018) 97–103, https://doi.org/10.1016/j.ultramic.2018.05.006.

32 H. Cho, J.W. Shin, R. Ryoo, Atomic scale mechanisms underlying thermal reshaping of anisotropic gold nanocrystals revealed by *in situ*, Electron Microsc., J. Phys. Chem. C. 124 (2020) 12855–12863, https://doi.org/10.1021/acs.jpcc.0c04281.

33 G. Kresse, J. Furthmüller, Efficiency of ab-initio total energy calculations for metals and semiconductors using a plane-wave basis set, Comp. Mater. Sci. 6 (1996) 15–50, https://doi.org/10.1016/0927-0256(96)00008-0.

34 J.P. Perdew, K. Burke, M. Ernzerhof, Generalized gradient approximation made simple, Phys. Rev. Lett. 77 (1996) 3865–3868, https://doi.org/10.1103/PhysRevLett.77.3865.

35 S.L. Dudarev, G.A. Botton, S.Y. Savrasov, C.J. Humphreys, A.P. Sutton, Electron-energy-loss spectra and the structural stability of nickel oxide: an LSDA+U study, Phys. Rev. B 57 (1998) 1505–1509, https://doi.org/10.1103/PhysRevB.57.1505.

36 A.E. Baber, X. Yang, H.Y. Kim, K. Mudiyanselage, M. Soldemo, J. Weissenrieder, S. D. Senanayake, A. Al-Mahboob, J.T. Sadowski, J. Evans, J.A. Rodriguez, P. Liu, F. M. Hoffmann, J.G. Chen, D.J. Stacchiolam, Stabilization of catalytically active Cu⁺ surface sites on titanium-copper mixed-oxide films, Angew. Chem. Int. Ed. 53 (2014) 5336–5340, https://doi.org/10.1002/anie.201402435.

37 A.K. Mishra, A. Roldan, N.H. de Leeuw, CuO surfaces and CO₂ activation: a dispersion-corrected DFT, U Study, J. Phys. Chem. C. 120 (2016) 2198–2214, https://doi.org/10.1021/acs.jpcc.5b10431.

38 P.E. Blochl, Projector augmented-wave method, Phys. Rev. B 50 (1994) 17953–17979.

39 S. Smidstrup, A. Pedersen, K. Stokbro, H. Jonsson, Improved initial guess for minimum energy path calculations, J. Chem. Phys. 140 (2014), 214106, https://doi.org/10.1103/PhysRevB.50.17953.

40 K. Mathew, R. Sundararaman, K. Letchworth-Weaver, T.A. Arias, R.G. Hennig, Implicit solvation model for density-functional study of nanocrystal surfaces and reaction pathways, J. Chem. Phys. 140 (2014), 084106, https://doi.org/10.1063/1.4865107.

41 H. Ha, S. Yoon, K. An, H.Y. Kim, Catalytic CO oxidation over Au nanoparticles supported on CeO₂ nanocrystals: effect of the Au–CeO₂ interface, ACS Catal. 8 (2018) 11491–11501, https://doi.org/10.1021/acscatal.8b03539.

42 H. An, H. Ha, M. Yoo, H.Y. Kim, Understanding the atomic-level process of CO-adsorption-driven surface segregation of Pd in (AuPd)₁₄₇ bimetallic nanoparticles, Nanoscale 9 (2017) 12077–12086, https://doi.org/10.1039/C7NR04435F.

43 N.E. Motl, E. Ewusi-Annan, I.T. Sines, L. Jensen, R.E. Schaak, Au-Cu alloy nanoparticles with tunable compositions and plasmonic properties: experimental

44 F. Gonella, G. Mattei, P. Mazzoldi, Au–Cu alloy nanoclusters in silica formed by ion implantation and annealing in reducing or oxidizing atmosphere, Appl. Phys. Lett. 75 (1999) 55–57, https://doi.org/10.1063/1.124275.

45 P. Sudipto, D. Goutam, Oriented Au–Cu nanoalloy particle incorporated SiO₂ film using new layer by layer deposition technique, J. Mater. Chem. 17 (2007) 493–498, https://doi.org/10.1039/B612539E.

46 W. Chen, R. Yu, L. Li, A. Wang, Q. Peng, Y. Li, A seed-based diffusion route to monodisperse intermetallic CuAu nanocrystals, Angew. Chem. Int. Ed. 49 (2010) 2917–2921, https://doi.org/10.1002/anie.200906835.

47 D. Kim, C. Xie, N. Becknell, Y. Yu, M. Karamad, K. Chan, E.J. Crumlin, J.K.N. ørskov, P. Yang, , Electrochemical activation of CO₂ through atomic ordering transformations of AuCu nanoparticles, J. Am. Chem. Soc. 139 (2017) 8329–8336, https://doi.org/10.1021/jacs.7b03516.

48 D. Kim, N. Becknell, Y. Yu, P. Yang, Room-temperature dynamics of vanishing copper nanoparticles supported on silica, Nano Lett. 17 (2017) 2732–2737, https://doi.org/10.1021/acs.nanolett.7b00942.

49 H. Lee, J. Lim, C. Lee, S. Back, K. An, J.W. Shin, R. Ryoo, Y. Jung, J.Y. Park, Boosting hot electron flux and catalytic activity at metal-oxide interfaces of PtCo bimetallic nanoparticles, Nat. Commun. 9 (2018) 2235, https://doi.org/10.1038/s41467-018-04713-8.

50 S. Tanuma, C.J. Powell, D.R. Penn, Calculations of electron inelastic mean free paths, Surf. Interface Anal. 17 (1991) 911–926, https://doi.org/10.1002/sia.740171304.

51 P. Jiang, D. Prendergast, F. Borondics, S. Porsgaard, L. Giovanetti, E. Pach, J. Newberg, H. Bluhm, F. Besenbacher, M. Salmeron, Experimental and theoretical investigation of the electronic structure of Cu₂O and CuO thin films on Cu(110) using X-ray photoelectron and absorption spectroscopy, J. Chem. Phys. 138 (2013), 024704, https://doi.org/10.1063/1.4773583.

52 D. Gamarra, G. Munuera, A.B. Hungría, M. Fernández-García, J.C. Conesa, P. A. Midgley, X.Q. Wang, J.C. Hanson, J.A. Rodríguez, A. Martínez-Arias, Structure–activity relationship in nanostructured copper–ceria-based preferential CO oxidation catalysts, J. Phys. Chem. C. 111 (2007) 11026–11038, https://doi.org/10.1021/jp072243k.

53 D. Gamarra, C. Belver, M. Fernández-García, A. Martínez-Arias, Selective CO oxidation in excess H2 over copper–ceria catalysts: identification of active entities/species, J. Am. Chem. Soc. 129 (2007) 12064–12065, https://doi.org/10.1021/ja073926g.

54 J. Schumann, J. Kröhnert, E. Frei, R. Schlögl, A. Truncschke, IR-spectroscopic study on the interface of Cu-based methanol synthesis catalysts: evidence for the formation of a ZnO overlayer, Top. Catal. 60 (2017) 1735–1743, https://doi.org/10.1007/s11244-017-0850-9.

55 L. Kang, B. Wang, A.T. Güntner, S. Xu, X. Wan, Y. Liu, S. Marlow, Y. Ren, D. Gianolio, C.C. Tang, V. Murzin, H. Asakura, Q. He, S. Guan, J.J. Velasco-Vélez, S.E. Pratsinis, Y. Guo, F.R. Wang, The electrophilicity of surface carbon species in the redox reactions of CuO-CeO₂ catalysts, Angew. Chem. Int. Ed. 60 (2021) 14420–14428, https://doi.org/10.1002/anie.202102570.

56 M.C. Biesinger, Advanced analysis of copper X-ray photoelectron spectra, Surf. Interface Anal. 49 (2017) 1325–1334, https://doi.org/10.1002/sia.6239.

57 H.Y. Kim, G. Henkelman, CO oxidation at the interface of Au nanoclusters and the stepped-CeO₂(111) surface by the Mars-van Krevelen mechanism, J. Phys. Chem. Lett. 4 (2013) 216–221, https://doi.org/10.1021/jz301778b.

58 R. Katal, S. Masudy-Panah, M. Sabbaghan, Z. Hossaini, M.H.D.A. Farahani, Photocatalytic degradation of triclosan by oxygen defected CuO thin film, Sep. Purif. Technol. 250 (2020), 117239, https://doi.org/10.1016/j.seppur.2020.117239.

59 H. Wang, Y. Guo, C. Li, H. Yu, K. Deng, Z. Wang, X. Li, Y. Xu, L. Wang, Cu/CuOₓ in-plane heterostructured nanosheet arrays with rich oxygen vacancies enhance nitrate electroreduction to ammonia, ACS Appl. Mater. Interfaces 14 (2022) 34761–34769, https://doi.org/10.1021/acsami.2c08534.

60 M. Shaw, D. Samanta, S. Bera, M. Kr Mahto, M.A.S. Shaik, S. Konar, I. Mondal, D. Dhara, A. Pathak, Role of surface oxygen vacancies and oxygen species on CuO nanostructured surfaces in model catalytic oxidation and reductions: insight into the structure–activity relationship toward the performance, Inorg. Chem. 61 (2022) 14568–14581, https://doi.org/10.1021/acs.inorgchem.2c01467.

61 M. Agrachev, S. Antonello, T. Dainese, M. Ruzzi, A. Zoleo, E. Aprà, N. Govind, A. Fortunelli, L. Sementa, F. Maran, Magnetic ordering in gold nanoclusters, ACS Omega 2 (2017) 2607–2617, https://doi.org/10.1021/acsomega.7b00472.

62 A.V. Kucherov, A.A. Slinkin, D.A. Kondrat'ev, T.N. Bondrarenko, A.M. Rubinstein, Kh.M. Minachev, Cu²⁺-cation location and reactivity in mordenite and ZSM–5: e.s.r.-study, Zeolites 5 (1985) 320–324, https://doi.org/10.1016/0144-2449(85)90166-6.

63 Y. Choi, S.K. Cha, S. Ha, S. Lee, H.K. Seo, J.Y. Lee, H.Y. Kim, S.O. Kim, W. Jung, Unravelling inherent electrocatalysis of mixed-conducting oxide activated by metal nanoparticle for fuel cell electrodes, Nat. Nanotechnol. 14 (2019) 245–251, https://doi.org/10.1038/s41565-019-0367-4.

64 M. Yoo, Y.-S. Yu, H. Ha, S. Lee, J.-S. Choi, S. Oh, E. Kang, H. Choi, H. An, K.-S. Lee, J. Y. Park, R. Celestre, M.A. Marcus, K. Nowrouzi, D. Taube, D.A. Shapiro, W. Jung, C. Kim, H.Y. Kim, A tailored oxide interface creates dense Pt single-atom catalysts with high catalytic activity, Energ. Environ. Sci. 13 (2020) 1231–1239, https://doi.org/10.1039/C9EE03492G.

65 T. Bunluesin, H. Cordatos, R.J. Gorte, Study of CO oxidation kinetics on Rh/Ceria, J. Catal. 157 (1995) 222–226, https://doi.org/10.1006/jcat.1995.1282.

66 H.C. Song, G.R. Lee, K. Jeon, H. Lee, S.W. Lee, Y.S. Jung, J.Y. Park, Engineering nanoscale interfaces of metal/oxide nanowires to control catalytic activity, ACS Nano 14 (2020) 8335–8342, https://doi.org/10.1021/acsnano.0c02347.